Mechano-electrochemistry effects due to deformation of copper oxide films

Denis Kramer[a], Yikun Wang[b], and Julian Wharton*[b]

Received Xth XXXXXXXXXX 20XX, Accepted Xth XXXXXXXXX 20XX
First published on the web Xth XXXXXXXXXX 200X
DOI: 10.1039/c000000x

In an attempt to elucidate the relationship and underlying processes of metal oxidation under stress, we combined electrochemical characterisation with Density-Functional-Theory (DFT) calculations to interrogate the (100) surface of copper. The oxidised (100) surface shows a missing-row reconstruction, which is believed to be driven by surface stress. Hence, additional mechanical stimuli might have significant impact onto the onset of Cu oxidation. We find that different surface sites respond differently to strain. O_{ads} at the thermodynamically favoured high-coordination hollow site (O coordinated with four Cu) is stabilised by up to 130 meV by imposing 2 % tensile strain onto the surface, while the low-coordination top site (O coordinated to one Cu) shows a markedly different sensitivity. Cramping into the hollow site, O_{ads} induces compressive stress into the (100) surface, an effect that is largely absent for adsorption at the top site. We also find that the thermodynamic advantage of reconstructive underpotential surface oxidation is diminished under tensile strain. Hence, imposing tensile stress counter-balances the oxygen induced surface stress, which might have an implication on the onset of bulk copper oxidation. Studying Cu (100) single crystal surfaces in perchloric acid using cyclic voltammetry, we were able to confirm sensitivity of the electrochemical response towards elastic strain.

1 Introduction

Bulk copper and surface oxidation has attracted immense interest over the years for the technical relevance as well as physical rich-

[a] *Engineering Materials, Engineering Sciences, University of Southampton, Hants., SO17 1BJ, UK.*
[b] *National Centre for Advanced Tribology at Southampton (nCATS), Engineering Sciences, University of Southampton, Hants., SO17 1BJ, UK; email: j.a.wharton@soton.ac.uk.*

ness involved[1–7]. Copper remains the material of choice for electric wires and is the industrial standard pipe material for various chemicals (e.g., refrigerants). In both cases, oxidation greatly threatens service performance by either reducing electrical conductivity or ductility. Copper oxidises to Cu_2O (cuprite) in neutral and alkaline media. In addition to being the oldest material for semiconductor electronics, Cu_2O finds new applications in diverse fields including nanoelectronics, spintronics, and photovoltaics. We, however, are mostly motivated by an interest to understand the corrosion behaviour of metalic copper under mechanical stress.

As a first step towards this goal, we focus here on the underpotential oxidation of the copper (100) surface, because forming oxide structures might act as precursors for bulk oxide film formation[8]. Numerous studies have elucidated the interaction of O_{ads} with copper surfaces and unveiled an intriguingly complex picture: (100) as well as (110) are fairly reactive and reconstruct in the presence of O_{ads}, while (111) is relatively inert. From the gas phase, O_2 dissociatively adsorbs at four-fold hollow sites (cf. inset of Figure 4 for an illustration of the adsorption mode), but a continuous $c(2\times2)$-O structure does not form. Instead, nanostructured $c(2\times2)$-O domains, separated by oxygen-deficient anti-phase boundaries, prevail up to a coverage of $\Theta\simeq 0.3$ ML. Larger $c(2\times2)$-O domains are unstable due to the accumulation of high stresses. The induced surface stress is the driving force for a $(2\sqrt{2}\times\sqrt{2})$R45°-O reconstruction in the gas-phase[9], where O_{ads} orders in a $c(2\times2)$-O super-structure, but every forth surface Cu row along [110] is missing. The ejected surface Cu forms nanometre-sized terraces onto which oxygen adsorbs as well[10].

Reconstruction of Cu(100) has also been observed in alkaline environments. At potentials above -810 mV vs. NHE, zigzag chains are observed, which are attributed to OH pulling Cu atoms out of the top layer and into the hollow site[11]. Two such Cu atoms are then linked by an OH group. The $c(2\times2)$ superstructure is reported to prevail in dilute acid[12].

2 Methodology

2.1 Theory

Total energy calculations. The use of Density-Functional-Theory (DFT) to investigate bulk phase stability[13], nano-particles[14], and surfaces[15,16] in aqueous environments has gained popularity over

the last years. We use DFT in the generalised gradient approximation (GGA) as parameterised by Perdew, Burke, and Ernzerhof[17] (PBE) and implemented via the projector augmented wave function method in the Vienna Ab-Initio Simulation Package (VASP)[18] to study the energetics of oxygen adsorption on Cu(100). Slabs were cut from the fully relaxed bulk with a lattice constant of 3.635 Å. We found that slabs consisting of eleven atomic Cu layers were sufficiently thick to mimic bulk behaviour in the interior of the slab. Atomic coordinates were allowed to relax, while the unit cell was fixed at dimensions equivalent to the fully relaxed bulk. The Brillion zone of the c(1x1) unit cell was sampled with a 9×9 Monkhorst mesh parallel to the surface. The mesh density was reduced appropriately for larger supercells. Only a single k-point is sampled perpendicular to the surface and a vacuum of at least 15 Å was maintained between slab images to minimize spurious interactions between slabs. Slabs were strained or compressed by adjusting the lattice constants appropriately to ensure isotropic strain parallel to the surface. Note that slab surfaces remain unstrained normal to the surface, because atomic coordinates were allowed to relax. We belief this to be in good agreement with experiment, where stress normal to the surface would imply a compensating backpressure of the aqueous phase.

Adsorption energies. To probe the energetics of oxygen adsorption, a simple difference scheme is used, where the total energy of a clean or reduced slab $E^{\mathrm{red}}_{\mathrm{slab}}$ is subtracted from the total energy of an oxidised slab $E^{\mathrm{ox}}_{\mathrm{slab}}$ with adatoms:

$$E_{\mathrm{ads,O}} = (E^{\mathrm{ox}}_{\mathrm{slab}} - E^{\mathrm{red}}_{\mathrm{slab}})/N_{\mathrm{O}} - (\mu_{\mathrm{O}} - \mu^{\circ}_{\mathrm{O}}) \qquad (1)$$

Note that the oxygen absorption energy depends on the oxygen chemical potential μ_O, reflecting the oxidative strength of the environment. For consistency with experiment, we choose to reference the oxygen chemical potential μ°_{O} to the oxygen dimer including a correction due to Wang *et al.* to compensate for inaccurate self-energy in the GGA of the O_2 dimer[19].

Surface Pourbaix diagrams. The thermodynamically favoured surface termination in aqueous environments is controlled by pH and potential. Surface Pourbaix diagrams, therefore, are a convenient tool. These can be obtained from DFT slab calculations to first approximation by reflecting the aqueous environment in a thermodynamic framework. Note that this is an approximation, because

it implicitly assumes that the interface (free) energies Metal—Aq. and Metal—Vac. have the same difference across terminations and therefore cancel when comparing terminations. The surface energy of a slab γ can be expressed as

$$(2A)\cdot\gamma = G_{\text{slab}} - \sum_i N_i \cdot \mu_i. \tag{2}$$

Note that the factor $2A$ is a consequence of the symmetry of the slab, which has two surfaces. The chemical potentials of the constituents μ_i are given by the equilibrium between the surface and bulk phases, namely the metal bulk and the aqueous phase. The surface energy can therefore be expressed as

$$(2A)\cdot\gamma = G_{\text{slab}} - N_{\text{Cu}}\cdot G_{\text{Cu}} - N_{\text{O}}\cdot\mu_{\text{O}} - N_{\text{H}}\cdot\mu_{\text{H}}, \tag{3}$$

if only oxygen- and hydrogen-containing species adsorb. The free energy of bulk copper is denoted by G_{Cu}. Neither μ_{O} nor μ_{H} are convenient variables, because they cannot be controlled independently in aqueous environments. Because water is a reactive species, the chemical potentials of oxygen and hydrogen are not independent variables and linked by

$$\mu_{\text{H}_2\text{O}} = 2\mu_{\text{H}} + \mu_{\text{O}}. \tag{4}$$

Finally, μ_{H} can be expressed as a linear combination of pH and voltage by

$$\mu_{\text{H}} = \mu_{\text{H}^+} - F\cdot\varphi. \tag{5}$$

Rewriting chemical potentials in Eq. 3 in terms of Eq. 4 and 5, a convenient expression for surface energy as function of pH and voltage is obtained:

$$\begin{aligned}(2A)\cdot\gamma = {} & G_{\text{slab}} - N_{\text{Cu}}\cdot G_{\text{Cu}} - N_{\text{O}}\cdot\mu_{\text{H}_2\text{O}} \\ & - (N_{\text{H}} - 2N_{\text{O}})(\mu_{\text{H}^+} - F\cdot\varphi),\end{aligned} \tag{6}$$

At room temperature, the proton chemical potential is simply given by $\mu_{\text{H}^+} = -0.0594\cdot\text{pH}$ if eV is used as units.

Equation 6 is linear in pH and voltage. Hence, the surface energy of each slab termination can be expressed as a plane in $(\gamma, \text{pH}, \varphi)$-space. The intersection of all planes representing possible terminations forms a convex hull, which after projection onto the (pH, φ)-plane can be visualised as a Pourbaix diagram. Finally, we neglect entropic contributions to the surface energy, which are likely to largely cancel between terminations, by calculating γ based on slab energies E_{slab} rather than slab free energies G_{slab}.

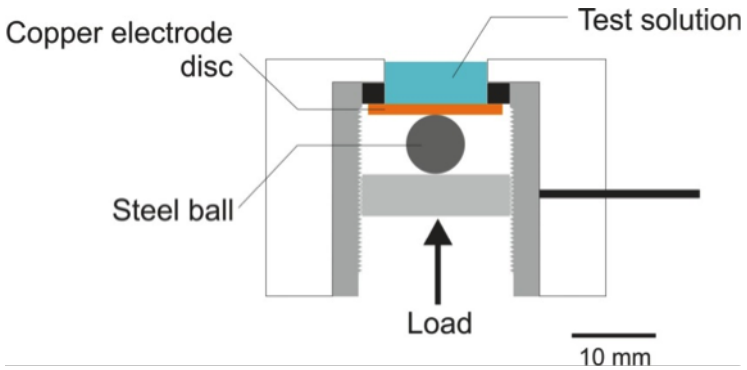

Fig. 1 Cross-sectional view of the experimental cell assembly detailing the setup for generating elastic stress at the copper surface.

2.2 Experimental

Electrodes and electrochemical cell. The experimental setup consisted of a single compartment three-electrode cell as sketched in Figure 1. Cyclic voltammetry (CV) was carried out with graphite rod and silver/silver chloride (Ag/AgCl, 3.5 M KCl, +0.205 V vs. NHE) counter and reference electrodes, respectively, using a Gamry Reference 600 potentiostat, Framework 6.25 and PHE200 Physical Electrochemical software. The working electrode disc was a Cu(100) single crystal (99.999 % Cu supplied by Goodfellow Cambridge Limited) with an exposed surface areas of $0.24\,cm^2$. Prior to electrochemical testing, the Cu electrode was mechanically polished to $1\,\mu m$, cleaned with acetone and then finally air dried. CVs were carried out in naturally aerated solution at a scan rate of $5\,mV/s$ with a step size of 2 mV, over a potential range of -741 mV to -241 mV vs. Ag/AgCl (-536 mV to -36 mV vs. NHE), in order to study the electrochemical response. Five CV scans were performed for each condition, and it is the data from the last cyclic scan that are reported here. CVs were carried out with and without elastic deformation to induce a tensile strain at the exposed electrode surface. Tensile stress was generated by positioning a steel ball bearing at the rear surface of the disc within the electrode assembly.

Chemicals. All the solutions were prepared with deionised water ($\geq$ 18.2 MΩcm, Millipore) using analytical grade chemicals (supplied by Sigma Aldrich). The test solution was 0.1 M $KClO_4$ (potassium chlorate) adjusted to pH 5 using perchloric acid ($HClO_4$).

coverage	ordering	site	$d(\mathrm{Cu-O})$ [Å]			$E_{\mathrm{ads,O}}$ [eV]		
			-2%	0%	2%	-2%	0%	2%
1 ML	$c(1\times1)$	hollow	1.88	1.88	1.88	-1.66	-1.80	-1.92
		bridge	1.81	1.80	1.80	-1.08	-1.13	-1.17
		top	1.77	1.76	1.76	-0.19	-0.18	-0.18
1/2 ML	$c(2\times2)$	hollow	1.94	1.95	1.96	-2.87	-2.92	-2.95
		bridge	1.80	1.80	1.80	-1.90	-1.94	-1.98
		top	1.78	1.73	1.72	-0.99	-0.92	-0.89

Table 1 Oxygen adsorption energies and Cu-O bond lengths on unreconstructed Cu(100) at different strains; negative strain corresponds to compression.

3 Results

3.1 Energetics of oxygen adsorption on unreconstructed Cu(100)

Adsorption energies of oxygen at different sites of the unreconstructed Cu(100) surface are given in Table 1; relative changes are visualised in Figure 2. We used a strain of 2 % to ensure that calculated effects are not obsured by numerical noise. Note that this is well outside the strain that can be sustained elastically by polycrystaline bulk copper, but is broadly in line with the large experimentally observed inward relaxation of Cu(100) of 1.0 % to 2.1 %[20–22] and surface stain in excess of 1 % that can be induced chemically[23]. Similarly large surface strain is observed at the beginning of epitaxial oxide growth on Cu(111), which was reported to exhibit 1.7 % compressive strain[24]. No plastic deformation, however, was observed in the slabs used in the DFT calculations, due to the defect-free single crystal nature of the computational domain. Adsorption energies under full coverage and 50% coverage in the $c(2\times2)$ configuration were calculated. Coulomb repulsion between surface oxygens is the main reason for the generally lower adsorption energies under half coverage. Adsorption energies show a clear trend with oxygen coordination. The four-fold coordinated hollow site provides the most stable absorption site in both cases, followed by the two-fold coordinated bridge site. The least stable adsorption site is the top site.

A single oxygen-copper bond is so unfavoured that the presence of oxygen triggers a substantial rumbling of the top copper layer for half coverage as can be seen from the insets of Figure 2. Rumbling refers to the outward relaxation of every other surface copper atom leading to a zig-zag configuration of the top copper layer as

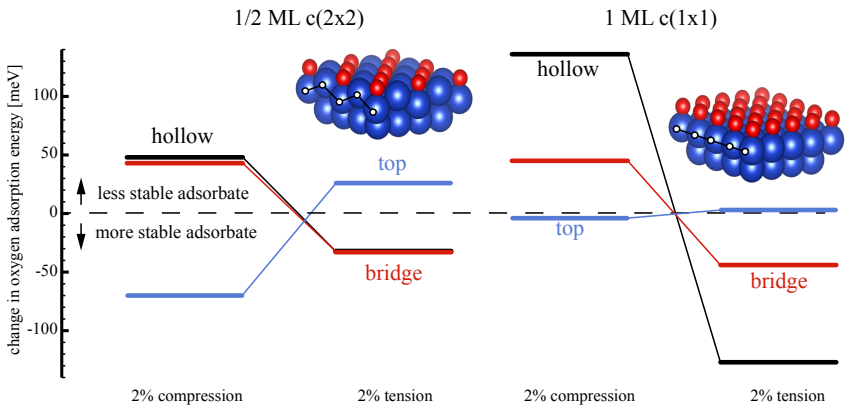

Fig. 2 Relative change of oxygen absoroption energies on unreconstructed Cu(100) under strain showing atypical behaviour of the top site; negative values correspond to stronger adsorption.

highlighted in the left inset of Figure 2. This substantial rumbling might also be the reason why the top site does not follow the trend of all other sites with respect to strain. It is the only site where tensile strain results in a destabilisation of adsorbed oxygen at $1/2$ ML coverage. For all other sites, tensile strain results in a stabilisation of up to 130 meV. As we will show later, stabilising a full monolayer of oxygen on Cu(100) requires more oxidating conditions than bulk copper can sustain. However, even at half coverage a stabilisation effect of about 50 meV is achieved for the important hollow site. The bridge site shows similar behaviour although this adsorption mode is extremely unlikely to be experimentally active due to the energetic cost of almost 1 eV relative to the hollow site.

It is worth noting that Cu-O bond distances are insensitive to strain. This can be rationalised by a scissor-like effect where oxygen relaxes inward if the top layer Cu-Cu distance increases and outward if the Cu-Cu distance decreases for the hollow and bridge site. Because oxygen coordinates with a single Cu atom at the top site at full coverage, we did not expect a sensitivity of the bond lengths in this case; but it is remarkable that the bond length at the top site remains roughly 1.75 Å at half coverage where the top Cu layer rumbles.

In summary, we find oxygen adsorption on the unreconstructed Cu(100) surface to be most favourable at the hollow site at half and full coverage. Putting the surface under tensile strain results in a stabilisation of adsorbed oxygen. The stabilisation effect increases with coverage from about 45 meV at $1/2$ ML to about 130 meV at

species	coverage	unit cell	reconst.	instability* [meV/Å^2]		
				$-2\,\%$	$0\,\%$	$2\,\%$
None	0	$c(1\times1)$	no	-	-	-
OH	$1/6$	$c(6\times2)$	yes		88	
	$1/2$	$c(2\times2)$	no	120	123	130
	1	$c(1\times1)$	no	360	343	320
O	$1/2$	$(2\sqrt{2}\times2)$R45°	yes	-	-	-
	$1/2$	$c(2\times2)$	no	8	4	<1
	1	$c(1\times1)$	no	-	-	-

* Distance from the convex hull is used as a measure of instability.

Table 2 Considered surface terminations of Cu(100) for construction of the unstrained surface Pourbaix diagram shown in Figure 3.

full coverage for $2\,\%$ tensile strain.

3.2 Thermodynamically favoured surface terminations

Unstrained Cu(100). The terminations given in Table 2 were considered to establish the thermodynamically most favourable surface termination as a function of pH and voltage. These were selected based on literature reports of Cu(100) surface studies in aqueous and gaseous environments as well as common structures. The resulting Pourbaix diagram is shown in Figure 3.

We find three terminations to be thermodynamically favoured and only two to be feasible within the bounds of bulk stability, which is indicated as shaded area in Figure 3. The unreconstructed clean surface is favoured at low voltages and pH. But oxygen adsorption becomes feasible well before bulk oxidation or dissolution occurs. We predict the missing row reconstruction to form above $-550\,$mV vs. NHE at pH 5, which is some $700\,$mV before bulk stability is compromised. We also predict that a full monolayer of oxygen would be thermodynamically feasible under extremely oxidising condition, but it is unlikely that this termination can be experimentally realised due to limited bulk stability of metallic copper.

It is also noteworthy that the $c(2\times2)-$O termination is very close in energy to become thermodynamically favoured. It is unstable by a mere $4\,\mathrm{meV/Å^2}$. Thermal energy is of the order of $25\,$meV at room temperature, making thermal activation of the $c(2\times2)-$O termination likely. We, therefore, consider it likely that oxygen adsorbs at the hollow site up to $0.5\,$ML with increasing voltage and remains in close competition with the missing row reconstruction

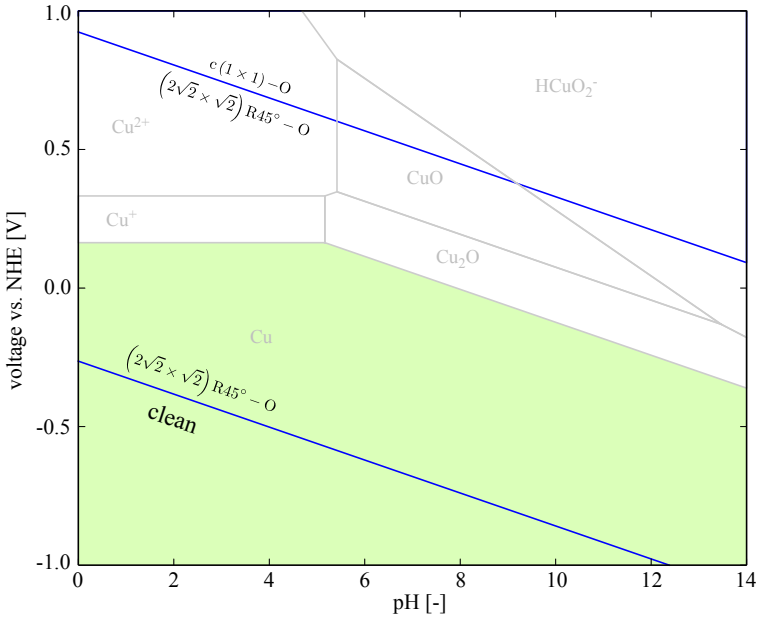

Fig. 3 DFT-derived surface Pourbaix diagram of thermodynamically favoured terminations of unstrained Cu(100) with long-range order. See Table 2 for considered terminations.

of the $(2\sqrt{2}\times 2)$R45° termination until bulk stability is lost.

Finally, our calculations indicate that neither of the considered OH orderings yields a termination low enough in energy to compete with the oxygen-terminated surfaces. In particular, our calculations indicate that the $c(6\times 2)-$OH model might not be the correct explanation of the zig-zag superstructure observed by Kunze et al. in alkaline media[11].

Cu(100) under tensile strain. We considered the same terminations given in Table 2 to investigate surface stability under tensile strain. The resulting Pourbaix diagram is very similar to the one shown in Figure 3 for the unstrained surface.

It should, however, be highlighted that the $c(2\times 2)-$O termination gains in stability relative to the missing row $(2\sqrt{2}\times 2)$R45° $-$O configuration. In fact, the competition is so close that we consider both terminations to be degenerate within the precision of our calculations. The energetics of oxygen adsorption at the hollow site are more sensitive towards strain than the three-fold coordinated adsorption site in the missing-row reconstruction. As shown in Figure 4, oxygen is stabilised by 30 meV in the four-fold coordinated

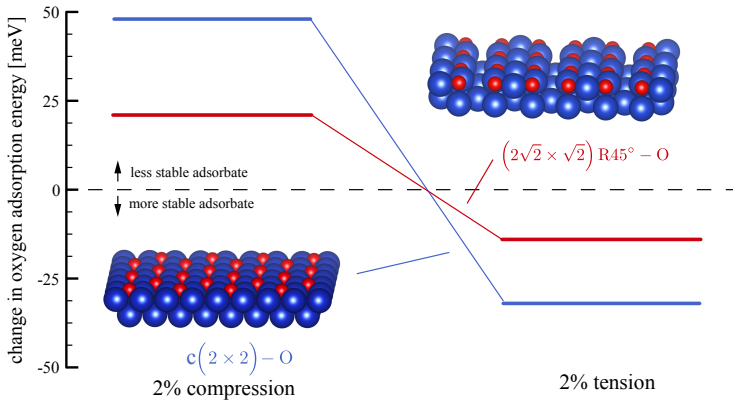

Fig. 4 Sensitivity of oxygen adsorption energies towards strain at unreconstructed and reconstructed (missing row) Cu(100); negative values correspond to stronger adsorption.

hollow site under 2 % strain, while the three-fold coordinated adsorption site in the missing row reconstruction only gains about half that energy.

This is in agreement with oxygen induced compressive surface stress. As the missing row reconstruction relieves at least part of the induced surface stress, it stands to reason that this termination benefits less from superimposing a tensile strain than the unreconstructed surface. That there is nonetheless an energetic benefit might indicate that the missing row reconstruction does not fully compensate for the induced surface stress.

3.3 Electrochemical response of Cu(100)

Figure 5 shows a pair of cyclic voltammograms for Cu(100) in 0.1 M $KClO_4$ (pH 5) spanning a potential region from −536 mV to −36 mV and return. The potential window was chosen such that H_2 evolution and Cu dissolution (bulk oxidation) is avoided. Two distinct reductive features (C1 and C2) are visible. while no clearly defined cathodic activity is seen up to −150 mV, where the onset of an oxidative process, possibly the beginning of bulk Cu dissolution, is detected. The C1 feature is at potentials of −300 mV and −318 mV vs. NHE, for a Cu (100) single crystal surface with and without imposed tensile stress, respectively. There is a positive shift in the order of 18 mV for this reductive surface process. The C2 feature at approximately 236 mV vs. NHE is most pronounced for the Cu(100) surface subject to tensile stress. Inspection by eye indicates that the C2 feature becomes somewhat more pronounced with

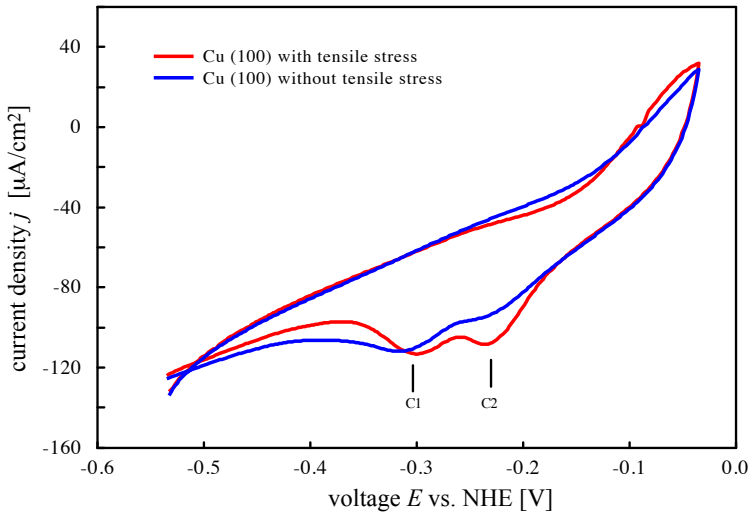

Fig. 5 Cyclic voltammogram of unstrained and elastically strained Cu(100) in 0.1 M $KClO_4$ adjusted to pH 5 using $HClO_4$; taken with a scan rate of 5 mV/s and a step size of 2 mV.

subjecting the surface to tensile stress. The large double layer capacity and general skew of the CVs make it hard to define a reliable base line for quantitative analysis of the charge associated with the two reductive processes.

4 Discussion

4.1 Underpotential oxidation of Cu(100)

The surface state and structure of copper in aqueous solutions is fundamentally important to understanding its corrosion performance, in addition to being of technologically importance in catalysis, electrodeposition and electronics. The characterisation of underpotential oxidation at the Cu(100) interface, however, is often sparsely discussed in the literature. Previous studies have suggested a surface reconstruction taking place in the underpotential range during the initial stages oxide formation[11,25,26]. Underpotential oxidation involves the electrosorption of oxygen species to form either very thin films or monolayer thick Cu_2O at potentials negative to the reversible potential of Cu_2O formation. This oxide structure is often considered as a precursor to Cu_2O growth.

Our DFT calculations and experimental results indicate substantial underpotential activity of Cu(100). While we calculate specific

adsorption of oxygen to happen above $-500\,\mathrm{mV}$ vs. NHE at pH 5, we measure surface activity at around $-300\,\mathrm{mV}$ vs. NHE. We consider the agreement between DFT prediction and experiment remarkable, in spite of the discrepancy of $200\,\mathrm{mV}$, given the rather crude approximations of the *First Principles* model: (1) no explicit treatment of the aqueous phases and (2) heuristic corrections of the reference states.

Kunze et al. also found electrochemical activity of Cu(100) in the underpotential region[11]. They, however, were able to detect an anodic as well as a cathodic peak around $-800\,\mathrm{mV}$ vs. NHE in $0.1\,\mathrm{M}$ NaOH. The activity at around $-300\,\mathrm{mV}$ vs. NHE reported here is in good agreement after compensating for the different pH values.

Kunze et al. were also able to detect substantial surface reconstruction in the underpotential region using scanning-tunneling-microscopy (STM), which they attributed to an interesting adsorption mode of OH leading to a zigzag feature within a $c(6\times2)$ superstructure. Our DFT results indicate that this model of the observed reconstruction is thermodynamically unlikely with the missing row reconstruction and the $c(2\times2)$ termination being thermodynamically significantly more favourable. Cruickshank et al. observed a $(\sqrt{2}\times\sqrt{2})\mathrm{R}45^\circ$ adsorbate superlattice on Cu(100) in acidic media that could not be detected on Cu(111)[12], which is in better agreement with our DFT predictions than the model of Kunze et al.

We, therefore, belief that Cu(100) reconstructs in perchloric acid environments similarly to the gas phase, and even if the resulting reconstruction differs somewhat from the missing row reconstruction, it is thermodynamically in close competition to it, likely to involve the removal of Cu atoms from the top layer, and might coexist with oxygen adsorption at the hollow site on unreconstructed Cu(100). Further, surface-enhanced Raman spectroscopy (SERS) data from Chan et al. indicates that the adsorbing species is indeed oxygen rather than hydroxide[27]. They detected a broad SERS band at $625\,\mathrm{cm}^{-1}$ which prevailed between -700 and $-100\,\mathrm{mV}$ vs. SCE in $0.1\,\mathrm{M}$ $\mathrm{HClO_4}$. This feature was attributed to $\mathrm{O_{ads}}$ after deuteration of the electrolyte failed to produce the redshift expected from hydrogenated adsorbates.

4.2 Double peak and asymmetry of cathodic and anodic characteristic

The CVs in Figure 5 have two original features that we were unable to link to previous literature: (1) the reductive double peak (C1 and

C2), and the apparently missing cathodic analogues.

It is noteworthy that the C2 feature is more sensitive to mechanical stimuli than the C1 feature. Given the close competition between oxygen adsorption at the hollow site of unreconstructed Cu(100) and in the missing row reconstruction predicted by our DFT calculations, it is tempting to attribute the C1 feature to one and the C2 feature to the other. Recalling that the three-fold adsorption site provided by the missing row reconstruction is slightly more stable, it is logical to attribute C1 to oxygen desorption from this site and C2 to desorption from the four-fold hollow site. This assignment is also in agreement with the relative growth of the C2 feature under tensile strain. As our DFT calculations indicate, adsorption on the hollow site benefits more from tensile strain, because of the higher compressive surface stress associated with this adsorption mode. Hence, it stands to reason that this mode gains in importance under tensile strain.

Our DFT calculations do not allow us to shed more light on the observed asymmetry between oxidative and reductive behaviour in the underpotential region, because a potential electrokinetic origin is not captured. However, it is not uncommon for oxidative surface processes to yield a substantially different response from their reductive counterparts, especially if a rearrangement of metal atoms is involved. The archetypal case is Pt, where surface oxidation is characterised by a plateau in CVs with some fine structure and the reduction back to a bare Pt surface by a marked peak similar to the ones seen in Figure 5. Ongoing research, therefore, focuses on linking the asymmetric behaviour to the reconstruction tendencies of Cu(100).

In addition, very little is known about the structural sensitivity of the cathodic processes on Cu single crystal surfaces[28]. It is generally well-established that the state of the Cu surface sites can influence the oxygen reduction reaction (ORR) reactivity, with the most reactive site towards oxygen redaction involving a Cu(I) species and the least reactive the metal itself, Cu(0)[29,30]. It is, therefore, possible that the stabilisation of the unreconstructed $c(2\times2)-\mathrm{O}$ termination under tensile strain might influence the kinetics of the ORR.

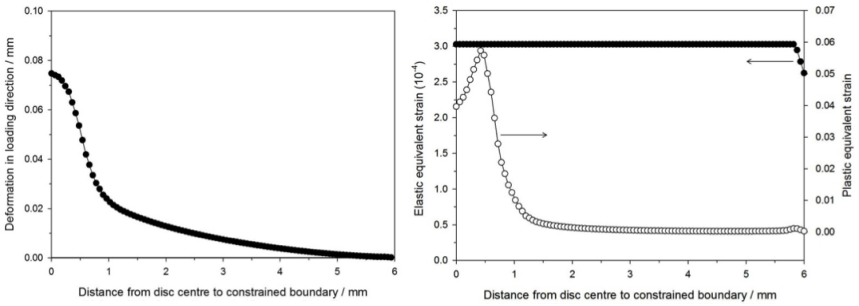

Fig. 6 Normal deformation and strain of the loaded Cu disc as estimated by Finite-Element Analysis.

5 Conclusion

Our work allows new understanding of the influence of mechanical induced strains on initial oxidation and reduction processes at a Cu(100) surface. We investigated the underpotential oxidation of Cu(100) as a function of mechanical stimuli. We find that surface stress induced by the adsorption of O_{ads} plays a crucial role in understanding the surface oxidation of Cu(100) and the electrochemical response in the underpotential region to strain. While oxidative surface stress is likely relieved via a reconstruction of the surface if no mechanical stimulus is applied, subjecting the surface to tensile strain diminishes the underlying driving force for reconstruction and brings oxygen adsorption at the unreconstructed surface (hollow site) on par with reconstructive oxygen adsorption. The stabilisation of a four-fold coordinated adsorption site under tensile stress might impact ORR kinetics, and we belief the close competition between the two adsorption modes to be the reason for the double peak in the CV data shown in Figure 5.

Appendix

A static finite element (FE) model was constructed to quantify the experimentally induced strain using ANSYS 14.0. The model consists of a copper disc (14 mm in diameter and thickness of 1 mm) in contact with a rigid ball bearing (7 mm in diameter). The copper disc was parameterised with a Youngs modulus of 110 GPa, a Poissons ratio of 0.343, a yield stress of 33.3 MPa and a tangent modulus of 0 GPa. The model considers material and geometric nonlinearities. Element SOLID185 with simplified enhanced strain formu-

lation (keyopt (2) = 3) and the contact element couple TARGE170 and CONTA175 were adopted to construct the 3D model. The behaviour of the contact surfaces between the disc and the ball were set to be standard. The disc is restrained on the 1 mm wide circumfence. The rigid ball was set to have an upward displacement of 0.1mm.

The von Mises strain (effective strain), ε_e, was determined using the following expression:

$$\varepsilon_e = \frac{1}{1+\nu}\sqrt{\frac{1}{2}\left[(\varepsilon_1-\varepsilon_2)^2+(\varepsilon_2-\varepsilon_3)^2+(\varepsilon_3-\varepsilon_1)^2\right]},$$

where ν is the effective Poissons ratio (0.5 for plastic strain) and ε_{1-3} are the principal strains.

The resultant deformation and strain distribution for 0.1 mm indention of the ball is shown in Figure 6. The plastic strain field induced by the ball is relatively localised in the centre of the disc with a peak value in excess of 5 % that falls off rather rapidly. Outside of an inner radius of $r_i = 1.5$ mm, the strain is mostly elastic. Given the relatively small fraction of surface where appreciable plastic deformation is expected, we consider it reasonable to assume that the electrochemical response discussed in Section 3.3 is largely dominated by elastic effects.

References

1 C. Ammon, A. Bayer, H. P. Steinrück and G. Held, *Chemical Physics Letters*, 2003, **377**, 163–169.

2 K. Bange, D. Grider, T. Madey and J. Sass, *Surface Science Letters*, 1984, **137**, A44.

3 A. B. Belonoshko and A. Rosengren, *Langmuir*, 2010, **102**, 8942–8952.

4 T. E. Eriksen, P. Ndalamba and I. Grenthe, *Corrosion Science*, 1989, **29**, 1241–1250.

5 G. Hultquist, P. Szakálos, M. J. Graham, A. B. Belonoshko, G. I. Sproule, L. Gråsjö, P. Dorogokupets, B. Danilov, T. Aastrup, G. Wikmark, G. K. Chuah, J. C. Eriksson and A. Rosengren, *Catalysis Letters*, 2009, **132**, 311–316.

6 A. Spitzer and H. Lüth, *Surface Science Letters*, 1982, **120**, A337–A338.

7 Q. L. Tang and Z. X. Chen, *Surface Science*, 2007, **601**, 954–964.

8 A. Soon, M. Todorova, B. Delley and C. Stampfl, *Surface Science*, 2007, **601**, 5809–5813.

9 F. Jensen, F. Besenbacher, E. Laegsgaard and I. Stensgaard, *Physical Review B*, 1990, **42**, 9206–9209.

10 K.-i. Tanaka, T. Fujita and Y. Okawa, *Surface Science*, 1998, **401**, L407–L412.

11 J. Kunze, V. Maurice, L. H. Klein, H.-H. Strehblow and P. Marcus, *Journal of Electroanalytical Chemistry*, 2003, **554-555**, 113–125.

12 B. J. Cruickshank, D. D. Sneddon and A. A. Gewirth, *Surface Science*, 1993, **281**, L308–L314.

13 K. A. Persson, B. Waldwick, P. Lazic and G. Ceder, *Physical Review B*, 2012, **85**, 235438.

14 B. C. Han, C. R. Miranda and G. ceder, *Physical Review B*, 2008, **77**, 1–9.

15 R. Benedek, M. M. Thackeray and A. van de Walle, *Journal Of Materials Chemistry*, 2009, **20**, 369.

16 H. A. Hansen, J. Rossmeisl and J. K. Norskov, *Physical Chemistry Chemical Physics*, 2008, **10**, 3722–3730.

17 J. P. Perdew, K. Burke and M. Ernzerhof, *Physical Review Letters*, 1996, **77**, 3865–3868.
18 G. Kresse and D. Joubert, *Physical Review B*, 1999, **59**, 1758–1775.
19 L. Wang, T. Maxisch and G. ceder, *Physical Review B*, 2006, **73**, 195107.
20 J. Wan, Y. L. Fan, D. W. Gong, S. G. Shen and X. Q. Fan, *Modelling and Simulation in Materials Science and Engineering*, 1999, **7**, 189.
21 H. Davis and J. Noonan, *Surface Science*, 1983, **126**, 245 – 252.
22 D. M. Lind, F. B. Dunning, G. K. Walters and H. L. Davis, *Phys. Rev. B*, 1987, **35**, 9037–9044.
23 D. Sekiba, Y. Yoshimoto, K. Nakatsuji, Y. Takagi, T. Iimori, S. Doi and F. Komori, *Phys. Rev. B*, 2007, **75**, 115404.
24 Y. S. Chu, I. K. Robinson and A. A. Gewirth, *The Journal of Chemical Physics*, 1999, **110**, 5952–5959.
25 V. Jovi and B. Jovi, *Journal of Electroanalytical Chemistry*, 2003, **541**, 13 – 21.
26 V. Maurice, H.-H. Strehblow and P. Marcus, *Surface Science*, 2000, **458**, 185 – 194.
27 H. Y. H. Chan, C. G. Takoudis and M. J. Weaver, *Journal of Physical Chemistry B*, 1999, **103**, 357–365.
28 T. Jiang and G. Brisard, *Electrochimica Acta*, 2007, **52**, 4487 – 4496.
29 F. King, M. Quinn and C. Litke, *Journal of Electroanalytical Chemistry*, 1995, **385**, 45 – 55.
30 G. Kear, B. Barker and F. Walsh, *Corrosion Science*, 2004, **46**, 109 – 135.

